Elastic FWI of the CAMI FRS 3D walkaway-walkaround VSP fiber survey: A synthetic case study

Matt Eaid, Scott Keating, Marie Macquet, and Kris Innanen

ABSTRACT

Distributed acoustic sensing could further enable reservoir monitoring by providing a means of acquiring repeatable seismic surveys. Monitoring during CO_2 sequestration is a key area where advancements in DAS monitoring will be beneficial. The containment and monitoring institute (CaMI) has a Field Research Station designed to explore technologies for this very purpose. In 2018 a baseline 3D walkaway-walkaround VSP was acquired with geophones, straight DAS fiber, and helical DAS fiber. In preparation for inverting this dataset and computing a baseline model for future time-lapse surveys, we examine the inversion of simulated datasets from synthetic models computed from field site well logs. A key component of this study is examination of various elastic model parameterizations and the effect they have on the quality of the inversions. Through our analysis we determine that all of the parameterizations tested produce reasonable inversion results, but a $Ip - Is - \rho$ paramaterization appears to be the most robust and is most successful in mitigating cross talk. These baseline inverted models are then used as starting models in an inversion from simulated data from models after 5 years of CO_2 injection. Using data from all three sensors types we are able to invert for the V_p anomaly induced by injection but struggle to invert for the V_s and ρ anomalies.

INTRODUCTION

Carbon capture and storage (CCS) has gained attention as a viable technology for reducing greenhouse gas emissions from electricity production and industrial processes. In CCS, carbon dioxide (CO_2) is captured during industrial processes, liquefied, and stored in depleted subsurface reservoirs. The in-situ CO_2 must be monitored to ensure that it is remaining in the target formation, and not migrating to the surface. Time-lapse seismic imaging is the premier technology for monitoring the CO_2 plume. In time-lapse seismic monitoring a baseline survey is acquired prior to injection of carbon dioxide, and then repeat surveys are acquired as often as desired to monitor the inferred migration of the CO_2 from changes in elastic subsurface parameters. It is crucial in time-lapse monitoring for the acquisition geometry to remain as consistent as possible so that changes in seismic data are directly related to elastic parameter perturbations caused by the presence of the gaseous CO_2.

Three-component geophones are the prevalent technology for acquiring seismic data. However, their size typically means that they cannot be placed in boreholes used for production or injection, without shutting in the well. The consequence of this is the drilling of dedicated monitor wells. A relatively new technology for seismic acquisition, which offers many benefits for time-lapse monitoring is distributed acoustic sensing (DAS). DAS employs telecommunications optical fibers for recording seismic strain data. The noninvasive nature of these fibers allows them to be placed in active injection wells, negating the requirement for dedicated monitoring wells. Additionally, the fibers are generally cemented behind casing, allowing for repeatable survey geometry. For these reasons, DAS has increasingly become an important technology for monitoring CO_2 sequestration (O'Brien, 2017; Bacci et al., 2017).

In 2018, CREWES in partnership with the Containment and Monitoring Institute (CaMI) acquired a 3D walkaway-walkaround VSP survey into 3C accelerometers, straight DAS fiber, and helical DAS fiber. This survey was acquired at the CaMI field research station (FRS) in Brooks, Alberta (Lawton et al., 2017; Gordon and Lawton, 2018), which has the main goal of injecting CO_2 into a subsurface reservoir and developing technologies to monitor it. The 2018 survey was acquired at a time when sufficiently small amounts of CO_2 had been injected, that it may be considered to be a baseline survey. In preparation for using elastic full waveform inversion (FWI) to invert the field data and produce baseline models of the field site, this paper is concerned with conducting synthetic tests to examine how different elastic parameterizations affect parameter resolution in FWI and provide an understanding of the expected results that might be obtained on the field data. Following from Pan et al. (2019), we use multiple elastic parameter resolutions and explore their influence on parameter resolution in FWI. The methods developed by Eaid et al. (2020) will be used to invert data from the simulated straight and helical DAS fiber data, to explore the resolution provided by each fiber. The most successful of these parameterization will be used to invert data acquired after 1 year and 5 years of simulated CO_2 injection (Macquet et al., 2019).

SIMULATION OF DAS DATA

The main goal of this paper is to understand the parameter resolution offered by FWI of the data from the straight helical fibers, and gain an understanding our ability to monitor the CO_2 plume. DAS employs optical fibers to infer measurements of the strain produced by passing seismic waves. As light traverses the fiber, a portion of it is backscattered by optical impurities in the fiber. In DAS sensing an interrogator unit analyzes the interference pattern of the light scattered from two separated portions of the fiber, and uses perturbations in the interference pattern to infer seismic strain occurring along the fiber, between the two scattering centers. However, due to the rigidity of the optical fibers, DAS is sensitive only to the normal-tangential component of strain ϵ_{tt}. Coupling these two ideas, the simulation of DAS data requires the modeling of elastic strain fields, and a bookkeeping of a spatially-variable coordinate geometry that describes the fiber tangent $\hat{t}(s)$ at each position along its arc-length s (Innanen and Eaid, 2017; Eaid et al., 2018).

Elastic strain field simulation

Following from Pratt (1990) the 2D displacement field is computed through solutions to the coupled system of equations,

$$\omega^2 \rho u_x + \frac{\partial}{\partial x}\left[\lambda\left(\frac{\partial u_x}{\partial x} + \frac{\partial u_z}{\partial z}\right) + 2\mu\frac{\partial u_x}{\partial_x}\right] + \frac{\partial}{\partial z}\left[\mu\left(\frac{\partial u_z}{\partial x} + \frac{\partial u_x}{\partial z}\right)\right] + s_x = 0 \tag{1a}$$

$$\omega^2 \rho u_z + \frac{\partial}{\partial z}\left[\lambda\left(\frac{\partial u_x}{\partial x} + \frac{\partial u_z}{\partial z}\right) + 2\mu\frac{\partial u_z}{\partial_z}\right] + \frac{\partial}{\partial x}\left[\mu\left(\frac{\partial u_z}{\partial x} + \frac{\partial u_x}{\partial z}\right)\right] + s_z = 0 \tag{1b}$$

where $u_x = u_x(x, z, \omega)$, and $u_z = u_z(x, z, \omega)$ are the x- and z-components of the frequency domain particle displacement; $\lambda = \lambda(x, z)$ and $mu = \mu(x, z)$ are the Láme parameters; ρ = $\rho(x, z)$ is the density; and s_x and s_z are x and z-components of the frequency domain source function. Solving equations (1a) and (1b) provides the x and z-components of the frequency domain particle displacements. The associated components of the strain field in the x-z plane, solved on a grid staggered from the displacement grid are,

$$\epsilon_{xx} = \frac{1}{2\Delta x}\big[u_x(x_{n+1}, z_{n+1}) - u_x(x_n, z_{n+1}) + u_x(x_{n+1}, z_n) - u_x(x_n, z_n)\big] \tag{2a}$$

$$\begin{aligned}\epsilon_{xz} =& \frac{1}{4\Delta x}\big[u_z(x_{n+1}, z_{n+1}) - u_z(x_n, z_{n+1}) + u_z(x_{n+1}, z_n) - u_z(x_n, z_n)\big] \\ &+ \frac{1}{4\Delta z}\big[u_x(x_{n+1}, z_{n+1}) - u_x(x_{n+1}, z_n) + u_x(x_n, z_{n+1}) - u_x(x_n, z_n)\big]\end{aligned} \tag{2b}$$

$$\epsilon_{zz} = \frac{1}{2\Delta z}\big[u_z(x_{n+1}, z_{n+1}) - u_z(x_{n+1}, z_n) + u_z(x_n, z_{n+1}) - u_z(x_n, z_n)\big]. \tag{2c}$$

Careful examination of equations (1a) and (1b) shows that the strain terms in equations (2a)-(2c) are computed while solving for the displacement components.

The DAS fiber is sensitive only to those portions of the Cartesian strain field which induce normal-tangential strains in the fiber. Computing this tangential component of the strain field requires definition of a locally variant Frenet-Serret coordinate system defined by the fibers tangent direction $\hat{\mathbf{t}}(s)$, its normal $\hat{\mathbf{n}}(s) = \mathbf{n}(s)/|\mathbf{n}(s)|$, where $\mathbf{n}(s) = d\hat{\mathbf{t}}(s)/ds$, and its binormal $\hat{\mathbf{b}}(s) = \hat{\mathbf{t}}(s) \times \hat{\mathbf{n}}(s)$. The strain tensor in the Frenet-Serret system is,

$$\epsilon_{tnb} = \mathbf{P}(s)\epsilon_{xyz}\mathbf{P}(s)^{\mathrm{T}} \tag{3}$$

where, the matrix

$$\mathbf{P}(s) = \begin{bmatrix} \hat{\mathbf{t}}(s)\cdot\hat{\mathbf{x}} & \hat{\mathbf{t}}(s)\cdot\hat{\mathbf{y}} & \hat{\mathbf{t}}(s)\cdot\hat{\mathbf{z}} \\ \hat{\mathbf{n}}(s)\cdot\hat{\mathbf{x}} & \hat{\mathbf{n}}(s)\cdot\hat{\mathbf{y}} & \hat{\mathbf{n}}(s)\cdot\hat{\mathbf{z}} \\ \hat{\mathbf{b}}(s)\cdot\hat{\mathbf{x}} & \hat{\mathbf{b}}(s)\cdot\hat{\mathbf{y}} & \hat{\mathbf{b}}(s)\cdot\hat{\mathbf{z}} \end{bmatrix} \tag{4}$$

is an operator projecting the strain field in Cartesian coordinates onto local fiber coordinates. Expansion of equation (3), with equation (4) gives the local DAS fiber response,

$$\epsilon_{tt} = (\hat{\mathbf{t}}\cdot\hat{\mathbf{x}})^2\epsilon_{xx} + 2(\hat{\mathbf{t}}\cdot\hat{\mathbf{x}})(\hat{\mathbf{t}}\cdot\hat{\mathbf{y}})\epsilon_{xy} + 2(\hat{\mathbf{t}}\cdot\hat{\mathbf{x}})(\hat{\mathbf{t}}\cdot\hat{\mathbf{z}})\epsilon_{xz} + (\hat{\mathbf{t}}\cdot\hat{\mathbf{y}})^2\epsilon_{yy} + 2(\hat{\mathbf{t}}\cdot\hat{\mathbf{y}})(\hat{\mathbf{t}}\cdot\hat{\mathbf{z}})\epsilon_{yz} + (\hat{\mathbf{t}}\cdot\hat{\mathbf{z}})^2\epsilon_{zz}. \tag{5}$$

In practice, to improve the signal-to-noise ratio the two scattering centers are separated by a length of fiber, where the length is referred to as the gauge length. All of the strain perturbations between the two scattering centers contribute to the change in the interference pattern, meaning DAS provides an average of the strain over the gauge length. At a fixed time t and position s along the fiber, the DAS datum is,

$$d(s) = \int_{-L/2}^{L/2} W(s - s', L)\epsilon_{tt}(s')ds' \tag{6}$$

where,

$$W(s, L) = \begin{cases} 1/L, & -L/2 < s < L/2 \\ 0, & \text{otherwise} \end{cases} . \tag{7}$$

FULL WAVEFORM INVERSION OF DAS DATA

The aim of FWI is to estimate the distribution of subsurface properties by minimizing an objective function of the form,

$$\phi = ||\mathbf{Ru}(\mathbf{m}) - \mathbf{d}||_2^2 \tag{8}$$

where **u** is the modeled wavefield as a function of the model parameters **m**, **R** is an operator transforming the modeled wavefield into measurements directly comparable to the observed data **d**. Minimization of equation (8), through the adjoint state method (Metivier et al., 2013) gives the gradient

$$\mathbf{g} = \frac{\partial \phi}{\partial \mathbf{m}} = \left\langle \frac{\partial \mathrm{S}}{\partial \mathbf{m}}\mathbf{u}, \lambda \right\rangle \tag{9}$$

where $lambda$ is the adjoint wavefield computed through solutions to,

$$\mathrm{S}^\dagger \lambda = \mathbf{R}^\dagger(\mathbf{Ru}(\mathbf{m}) - d) \tag{10}$$

and where S is a wave equation operator (e.g. Marfurt, 1984).

In conventional FWI of geophone data, the matrix **R** has the sole purpose of sampling the displacement wavefield at the location of the receivers which recorded the observed data. However, no assumption is enforced on the form that **R** must take in full waveform inversion. We are free to allow **R** to take on an expanded role without affecting the form of the objective function in equation (8) or the gradient in equation (9). Eaid et al. (2020) show that by allowing **R** to handle the properties of DAS receivers, that is compute the localized strain response, project it onto the fiber tangent, and invoke gauge length averaging, the conventional equations used in FWI can readily be extended to FWI of DAS data.

Elastic FWI parameterizations

The elastic wave equation expressed by equations (1a) and (1b) can be written as,

$$\rho\omega^2\mathbf{u} + (\lambda+2\mu)\nabla(\nabla\cdot\mathbf{u}) - \mu\nabla\times(\nabla\times\mathbf{u}) + \nabla\lambda(\nabla\cdot\mathbf{u}) + \nabla\mu(\nabla\mathbf{u}+\nabla\mathbf{u}^{\mathrm{T}}) + \mathbf{f} = 0. \quad (11)$$

Using the elastic stress-strain relation, equation (11) can be re-parmeterized using the elastic stiffness tensor components $c_{11} = (\lambda + 2\mu)$, $c_{44} = \mu$, and $c_{13} = \lambda = c_{11} - 2c_{44}$. Replacing the parameters in equation (11) with the stiffness tensor components provides the wave equation for a heterogeneous isotropic-elastic medium defined in terms of the stiffness tensor,

$$\rho\omega^2\mathbf{u} + c_{11}\nabla(\nabla\cdot\mathbf{u}) - c_{44}\nabla\times(\nabla\times\mathbf{u}) + \nabla(c_{11}-2c_{44})(\nabla\cdot\mathbf{u}) + \nabla c_{44}(\nabla\mathbf{u}+\nabla\mathbf{u}^{\mathrm{T}}) + \mathbf{f} = 0. \quad (12)$$

Equation (12) is a function of the parameters c_{11}, c_{44}, and ρ, and their spatial derivatives $\nabla c_{11}, \nabla c_{44}$, and $\nabla\rho$. This form of the elastic wave equation allows us to reparameterize it in terms of any set of elastic parameters, by writing the parameters c_{11}, c_{44}, and ρ in terms of the chosen set of elastic parameters. The gradient, and Hessian in FWI contain terms of the form $\partial \mathrm{S}/\partial m$, meaning to include different parameterizations in FWI, we also require derivatives of the parameters c_{11}, c_{44}, and ρ in terms of the chosen model parameters. In this paper we will consider the four elastic parameterizations $(1/v_p^2, 1/v_s^2, \rho)$, (v_p, v_s, I_p), (v_p, v_s, I_s), and (I_p, I_s, ρ). Table 1 summarizes the definitions of c_{11}, c_{44}, and ρ in terms of the model parameters for each of the four parameterizations, and the their derivatives with respect to the chosen model parameters.

Each of these parameterizations have different sensitivity kernels (Pan et al., 2019), and as a result perturbations in each parameter result in different character in the scattered wavefield. The angular variation in the wavefield scattered by a perturbation in a given parameter is an important control on the parameter resolution afforded by a given acquisition geometry in FWI. Additionally, if two parameters are to be uniquely determined, then their scattered wavefields should be minimally correlated over the acquisitions apertures in the survey. If they are not, then the variation in the wavefield produced by one parameter can be erroneously associated with another leading to poor model updates; this situation is known as cross-talk.

Scattering radiation patterns

Scattering radiation patterns,

$$\frac{\partial\mathbf{u}}{\partial\mathbf{m}} \approx \frac{\mathbf{u}(\mathbf{m}+\delta\mathbf{m}) - \mathbf{u}(\mathbf{m})}{\delta\mathbf{m}} \quad (13)$$

which describe the sensitvity of the wavefield to perturbations in a model parameter **m**, are an important tool for diagnosing challenges that may arise due to parameter resolution and

Table 1. Summary of the definitions of c_{11}, c_{44}, and ρ and their derivatives in terms of the chose parameterizations.

Parameters	c_{11}	c_{44}	ρ		∂c_{11}	∂c_{44}	$\partial \rho$
$\frac{1}{v_p^2}$-$\frac{1}{v_s^2}$-ρ	$(v_p^{-2})^{-1}\rho$	$(v_s^{-2})^{-1}\rho$	ρ	∂v_p^{-2}	$-\rho/v_p^4$	0	0
				∂v_s^{-2}	0	$-\rho/v_s^4$	0
				$\partial \rho$	$(v_p^{-2})^{-1}$	$(v_s^{-2})^{-1}$	1
v_p-v_s-I_p	$v_p I_p$	$\frac{v_s^2}{v_p} I_p$	$\frac{I_p}{v_p}$	∂v_p	I_p	$-(v_s^2/v_p^2)I_p$	$-I_p/v_p^2$
				∂v_s	0	$2(v_s/v_p)I_p$	0
				∂I_p	v_p	v_s^2/v_p	$1/v_p$
v_p-v_s-I_s	$\frac{v_p^2}{v_s} I_s$	$v_s I_s$	$\frac{I_s}{v_s}$	∂v_p	$2(v_p/v_s)I_s$	0	0
				∂v_s	$\text{-}(v_p^2/v_s^2)I_s$	I_s	$-I_s/v_s^2$
				∂I_s	v_p^2/v_s	v_s	$1/v_s$
I_p-I_s-ρ	$\frac{I_p^2}{\rho}$	$\frac{I_s^2}{\rho}$	ρ	∂I_p	$2I_p/\rho$	0	0
				∂I_s	0	$2I_s/\rho$	0
				$\partial \rho$	$-(I_p^2/\rho^2)$	$-(I_p^2/\rho^2)$	1

cross-talk. Consider a reference medium that is homogeneous in the chosen set of model parameters p_1, p_2, and p_3, and a perturbed medium containing a single point perturbation in one of the three model parameters. Wavefields $\mathbf{u}(\mathbf{m})$ and $\mathbf{u}(\mathbf{m}+\delta\mathbf{m})$ are propagated through the reference and perturbed medium, and the scattering radiation patterns in equation (13) are computed through the difference of these two wavefields. The resulting scattering radiation pattern describes the energy scattered by the point perturbation as a function of the opening angle between the source and receiver.

These radiation patterns are important tools for examining parameter resolution and cross-talk in FWI. In order to resolve a given parameter then our acquisition must supply opening angles that record a sufficient amount of the energy scattered by perturbations in that parameter. To suppress cross-talk in our inversions the radiation patterns between two parameters should minimally correlated over our acquisition aperture. If they are not, then two parameters will produce similar scattering of the wavefield, and independently resolving each parameter will be challenging if not impossible. Each parameterization scatters the wavefield in different ways, and analysis of there scattering radiation patterns can help select potentially successful parameterizations and diagnose challenges that arise in the inversion due to cross-talk and parameter resolution.

Figures 1(a)-1(b) plots the u_x and u_z wavefields scattered by a perturbation in V_p, Figures 1(c)-1(d) for a perturbation in V_s, and Figures 1(e)-1(f) for a perturbation in ρ. Figures 1(g)-1(i) plots the ϵ_{xx}, ϵ_{xz}, and ϵ_{zz} wavefields scattered by a perturbation in V_p, Figures 1(l)-1(n) for perturbations in V_s, and Figures 1(q)-1(s) for perturbations in ρ. Figures 1(j), 1(o), and 1(t) plot the composite radiation pattern that a straight fiber is sensitive to, and Figures 1(k), 1(p), and 1(u) plot the composite radiation pattern that the 30-degree helical fiber is sensitive to. Figures 2, 3, and 4 plot the same for the $V_p - V_s - \rho$ parameterization. The composite radiation patterns are formed through a weighted sum of the ϵ_{xx}, ϵ_{xz}, and ϵ_{zz} radiation patterns where the weights on the sum are a function of the fiber geometry, and are equal to the coefficients on the strain components in equation (5).

These radiation patterns provide insights into which model parameterizations may lead to more successful inversions using geophones, straight fibers, and 30-degree helical fibers in VSP geometries. For the maximum offset of 500 meters and depth of 400 meters considered in our study, the maximum opening angle between source and receiver for reflected energy is approximately 40-degrees. If two model parameters scatter energy in a similar way over these opening angles then it will be challenging to resolve each parameter independently using reflected energy and cross-talk becomes a concern. A significant benefit of VSP acquisition is that we also gain access to transmitted energy represented by the bottom half of the radiation patterns. Examination of the radiation patterns shows that many parameter combinations that scatter in a similar way at reflection angles have very different scattering patterns at transmission angles. Successful parameterizations should scatter significant energy at transmitted angles, at near-to-intermediate reflection angles (0-40 degrees), and should have minimally correlated scattering patterns in each parameter. Comparison of the radiation patterns suggest that V_p-V_s-I_p, and I_p-I_s-ρ parameterizations may be better at coping with challenges related to parameter resolution and cross-talk. Both parameterizations scatter significant energy over the opening angles provided by the proposed acquisition geometry, and have minimally correlated scattering radiation patterns for

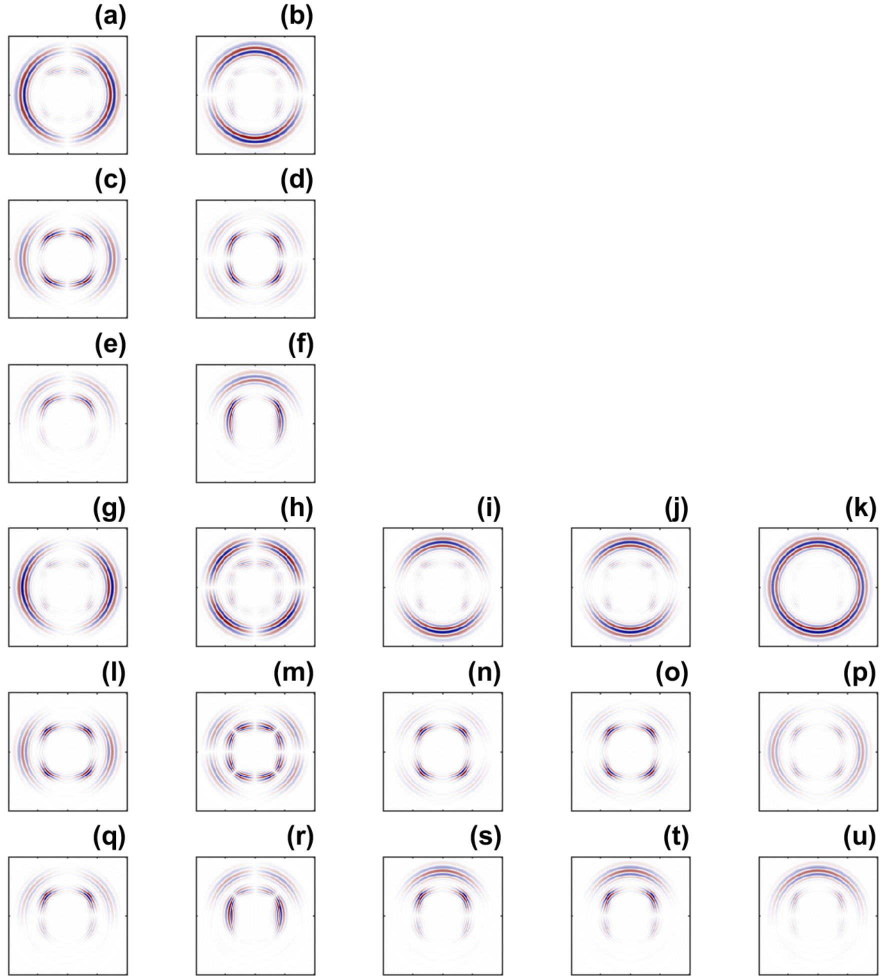

FIG. 1. Radiation patterns for the $1/v_p^2$-$1/v_s^2$-ρ parameterization. (a)-(b) u_x and u_z wavefields scattered by perturbations in v_p, (c)-(d) u_x and u_z wavefields scattered by perturbations in v_s, and (e)-(f) u_x and u_z wavefields scattered by perturbations in ρ. (g)-(i) ϵ_{xx}, ϵ_{xz}, and ϵ_{zz} wavefields scattered by perturbations in v_p, (l)-(n) ϵ_{xx}, ϵ_{xz}, and ϵ_{zz} wavefields scattered by perturbations in v_s, and (q)-(s) ϵ_{xx}, ϵ_{xz}, and ϵ_{zz} wavefields scattered by perturbations in ρ. (j), (o), and (t) Composite radaition patterns for the straight fiber. (k), (p), and (u) Composite radaition patterns for the 30-degree helical fiber.

all three parameters.

SYNTHETIC FWI OF CAMI DAS DATA

2018 CaMI FRS 3D walkaway-walkaround VSP

The CaMI FRS is located in Newell County, Alberta approximately 200km southeast of Calgary, Alberta. This site was developed with the goal of injecting CO_2 of a period of five years into the Basal Belly River reservoir at a depth of approximately 300 meters, and then

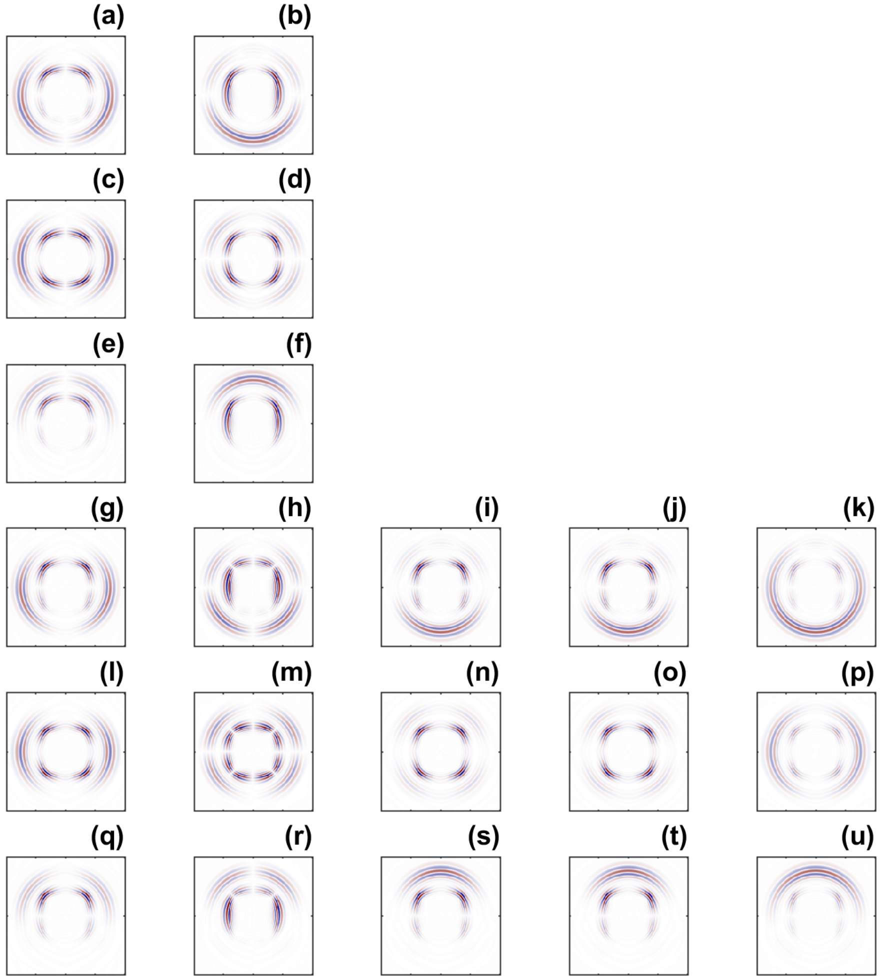

FIG. 2. Radiation patterns for the v_p-v_s-I_p parameterization. (a)-(b) u_x and u_z wavefields scattered by perturbations in v_p, (c)-(d) u_x and u_z wavefields scattered by perturbations in v_s, and (e)-(f) u_x and u_z wavefields scattered by perturbations in I_p. (g)-(i) ϵ_{xx}, ϵ_{xz}, and ϵ_{zz} wavefields scattered by perturbations in v_p, (l)-(n) ϵ_{xx}, ϵ_{xz}, and ϵ_{zz} wavefields scattered by perturbations in v_s, and (q)-(s) ϵ_{xx}, ϵ_{xz}, and ϵ_{zz} wavefields scattered by perturbations in I_p. (j), (o), and (t) Composite radaition patterns for the straight fiber. (k), (p), and (u) Composite radaition patterns for the 30-degree helical fiber.

monitor the injected CO_2 plume migration. Offset 20 meters southwest of the injection well is observation well two, commonly referred to as the geophysics well. This well is permanently outfit with down-going and up-going loops of straight and helical DAS fiber with a lead angle of 30º to a depth of 324 meters. The 2018 VSP was also acquired with 324 levels of 3C accelerometers spaced at one meter in observation well two. The seismic data were generated with an EnviroVibe minivib using a 1-150Hz linear sweep with 513 shots along 15 degree intervals on concentric circles. The source geometry is plotted in Figure 5.

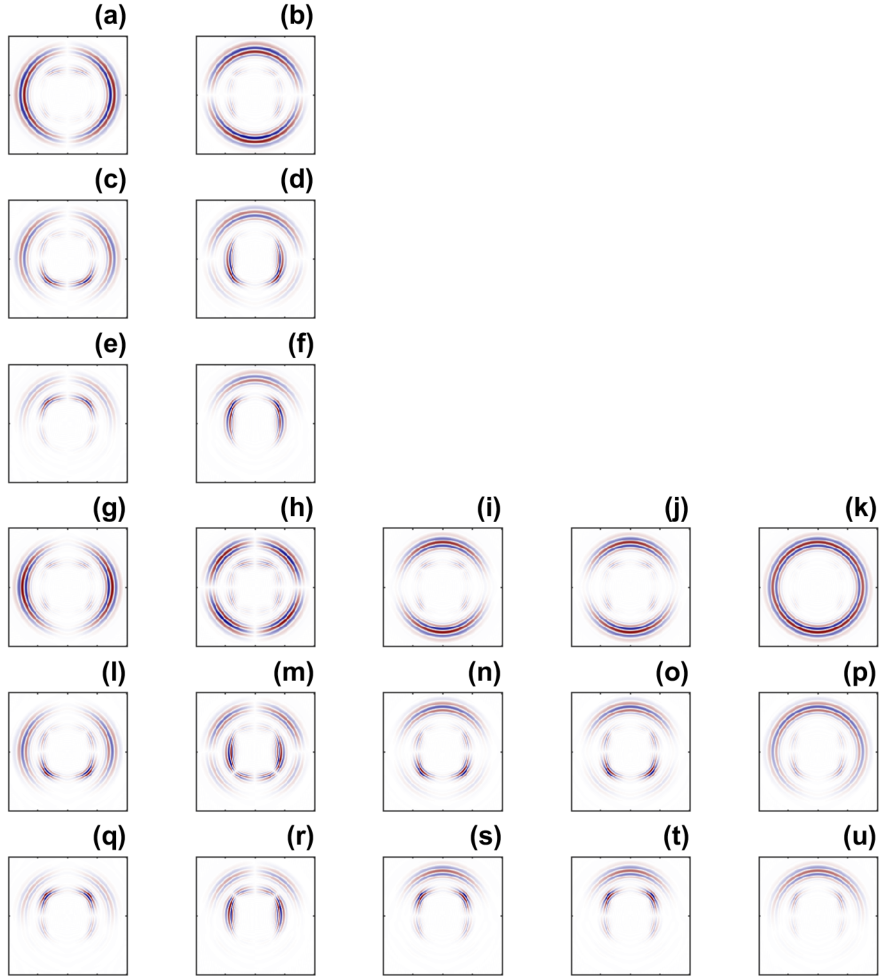

FIG. 3. Radiation patterns for the v_p-v_s-I_s parameterization. (a)-(b) u_x and u_z wavefields scattered by perturbations in v_p, (c)-(d) u_x and u_z wavefields scattered by perturbations in v_s, and (e)-(f) u_x and u_z wavefields scattered by perturbations in I_s. (g)-(i) ϵ_{xx}, ϵ_{xz}, and ϵ_{zz} wavefields scattered by perturbations in v_p, (l)-(n) ϵ_{xx}, ϵ_{xz}, and ϵ_{zz} wavefields scattered by perturbations in v_s, and (q)-(s) ϵ_{xx}, ϵ_{xz}, and ϵ_{zz} wavefields scattered by perturbations in I_s. (j), (o), and (t) Composite radaition patterns for the straight fiber. (k), (p), and (u) Composite radaition patterns for the 30-degree helical fiber.

This survey was acquired with 324 3C accelerometers, spaced at one meter depth intervals, a straight DAS fiber, and a helical DAS fiber with a 30-degree lead angle.

The injector well has compressional sonic, shear sonic, and density logs from 223-535 meters, while the geophysics well has compressional sonic logs from 61-336 meter depth. The two compressional sonic logs in each well are strongly correlated in their overlapping sections, and both are used to construct a single well log from 0-535 meters depth. Logs for the shear-velocity and density in the shallow section (0-223 meters) are constructed using linear regression, and power-regression respectively on cross-plots of P-wave velocity (V_p)

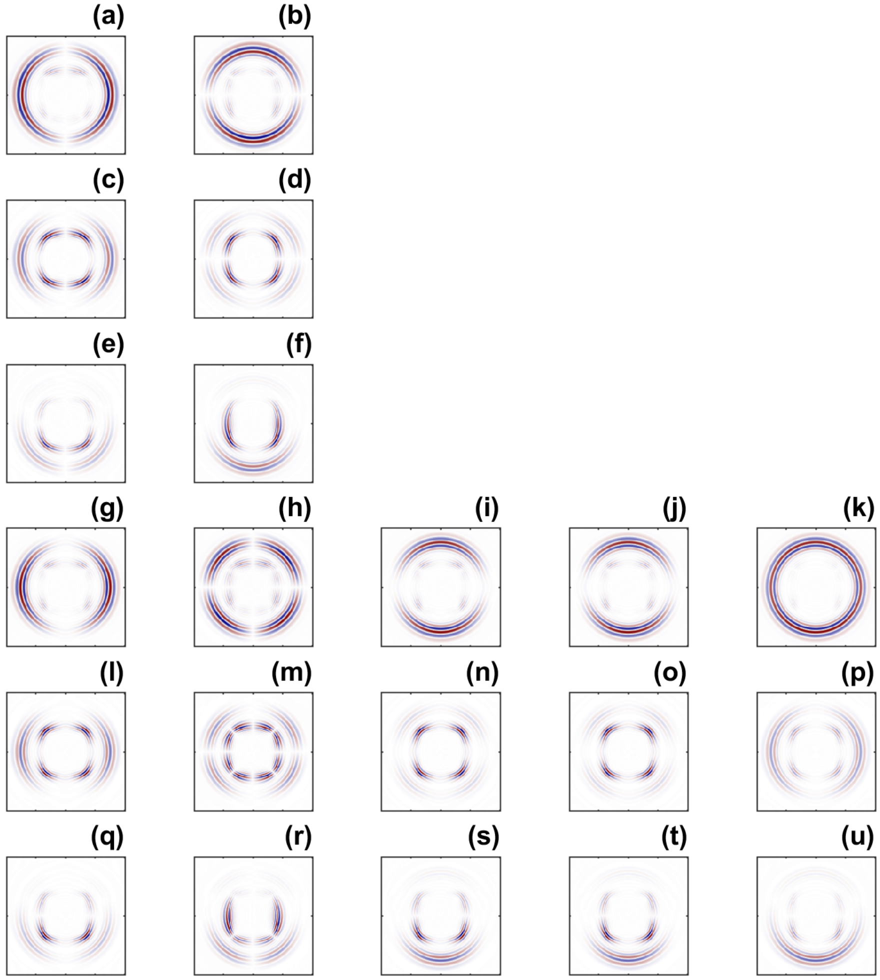

FIG. 4. Radiation patterns for the I_p-I_s-ρ parameterization. (a)-(b) u_x and u_z wavefields scattered by perturbations in I_p, (c)-(d) u_x and u_z wavefields scattered by perturbations in I_s, and (e)-(f) u_x and u_z wavefields scattered by perturbations in ρ. (g)-(i) ϵ_{xx}, ϵ_{xz}, and ϵ_{zz} wavefields scattered by perturbations in I_p, (l)-(n) ϵ_{xx}, ϵ_{xz}, and ϵ_{zz} wavefields scattered by perturbations in I_s, and (q)-(s) ϵ_{xx}, ϵ_{xz}, and ϵ_{zz} wavefields scattered by perturbations in ρ. (j), (o), and (t) Composite radaition patterns for the straight fiber. (k), (p), and (u) Composite radaition patterns for the 30-degree helical fiber.

versus S-wave velocity (V_s) and v_p versus density (ρ) from the logs in the deeper (223-535 meter) section. Figure 6a plots the cross-plot for V_p and V_s, and Figure 6b plots the cross-plot for v_p and ρ, where the red lines are the lines of best fit with equations

$$v_p = 1.07v_s + 1416.12 \tag{14a}$$

$$\rho = 159.69v_p^{0.34}. \tag{14b}$$

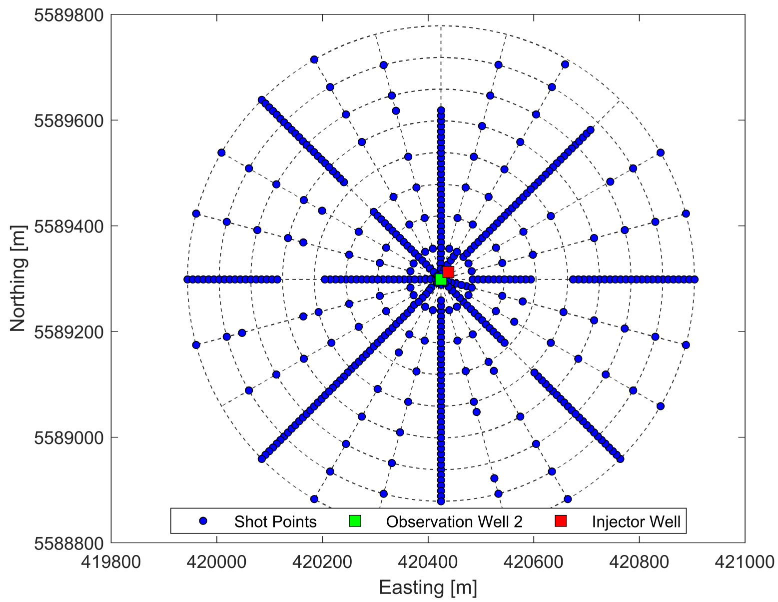

FIG. 5. Source geometry for the 2018 walkaway-walkaround VSP. Shot points are marked by the blue circles and are centered on observation well two marked by the green square. The injector well is marked by the red square.

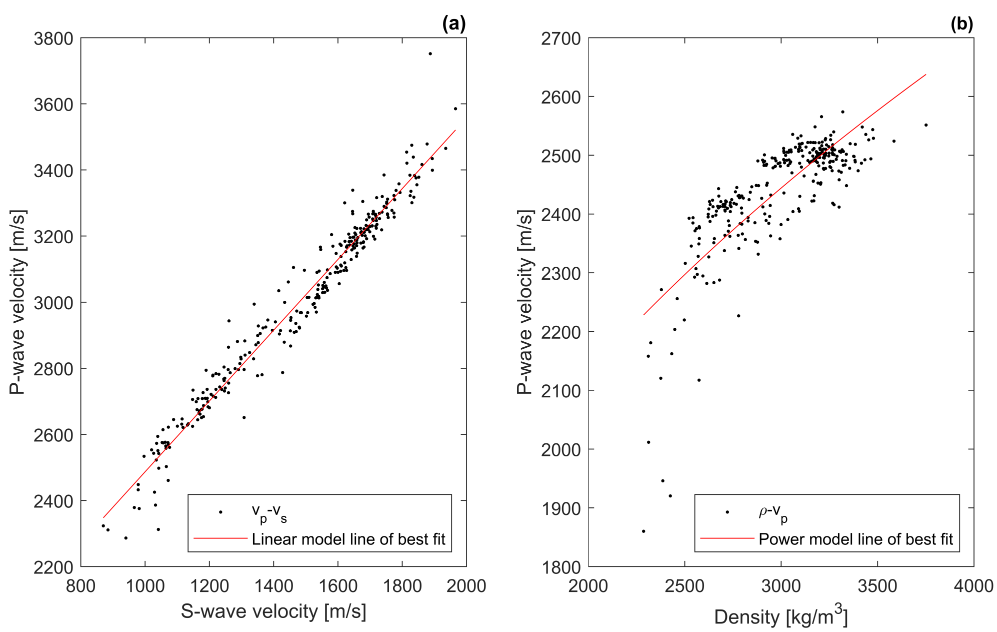

FIG. 6. (a) Cross-plot of V_p versus V_s and (b) cross-plot of V_p versus ρ for the log measurements in the injector well from 223-535 meters. The red lines are the linear regression and power model lines of best fit.

Figure 7a-7c plots the well logs for V_p, V_s, and ρ. The black lines are the acquired well logs, and the blue lines are the well logs blocked to 2.5 meters, which is the grid spacing we will use for finite difference simulations. The dashed red lines are the top and based of the Basal Belly River formation, targeted for CO_2 injection.

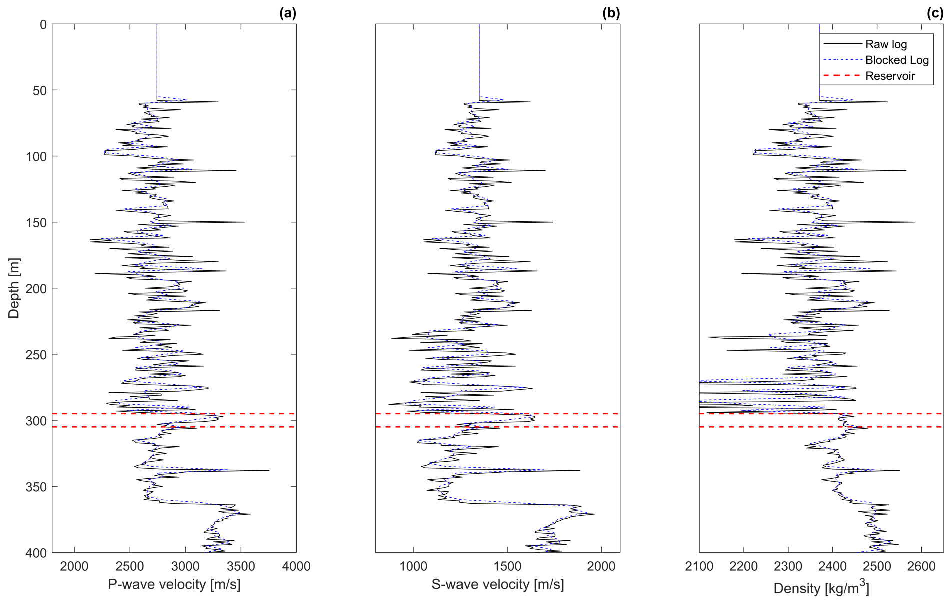

FIG. 7. (a) V_p well log, (b) V_s well log, and (c) ρ well log. The dotted-red lines are the top and base of the target Basal Belly River reservoir, the black line are the acquired well logs, and the blue line is the well log blocked to the 2.5 meter interval that will be used for finite difference simulations within FWI.

The blocked well logs in Figures 7a-7c are used to construct initial baseline models prior to CO_2 injection. Figures 8a-8e plot the starting V_p, V_s, ρ, I_p, and I_s models and 8f-8f plot the true baseline models derived from the well logs prior to injection for V_p, V_s, ρ, I_p, and I_s. Data are generated from these models using the 3D-VSP source line plotted in blue in Figure 9. The sources are treated as explosive in this study and are simulated with the seven frequency bands of [5-10Hz],[5-18.3Hz],[5-26.7Hz],[5-35Hz],[5-43.3Hz], and [5-60Hz] with each band consisting of five evenly spaced frequencies.

The generated data are recorded with 116 geophones spaced at 2.5 meters from 40-330 meter depth, a straight DAS fiber, and 30-degree helical fiber, located at the position of the observation well, 500 meters from the left edge of the model. The data are inverted with seven iterations of the truncated Gauss Newton optimization over the same frequency bands used to generate the data. The Hessian is approximated with a maximum of 20 iterations of the L-BFGS algorithm for each frequency band. The starting models are generated by smoothing the true models using a Gaussian smoother with a half-width of 50 meters. Figures 10(a)-10(e) plot the inverted models for V_p, V_s, ρ, I_p, and I_s for the $1/V_p^2$-$1/V_s^2$-ρ parameterization, Figures 10(f)-10(j) for the V_p-V_s-I_p parameterization, Figures 10(k)-10(o) for the V_p-V_s-I_s parameterization, and Figures 10(p)-10(t) for the I_p-I_s-ρ parameterization. Figure 11(a)-11(e) compares the inverted models for the $1/V_p^2$-$1/V_s^2$-ρ (green) and I_p-I_s-ρ (red) at the well location, and Figure 11(a)-11(e) compares the inverted models for the V_p-V_s-I_p (magenta) and V_p-V_s-I_s (blue). All of the parameterizations lead to similar recovery of the reservoir targeted for CO_2 sequestration, but the profiles in figure 11 suggest that the I_p-I_s-rho (red) parameterization is the most successful at avoiding cross-talk. This is apparent on the density inversion which is a better match to the true models than any of the other parameterizations. This is the only parameterization that gets information about

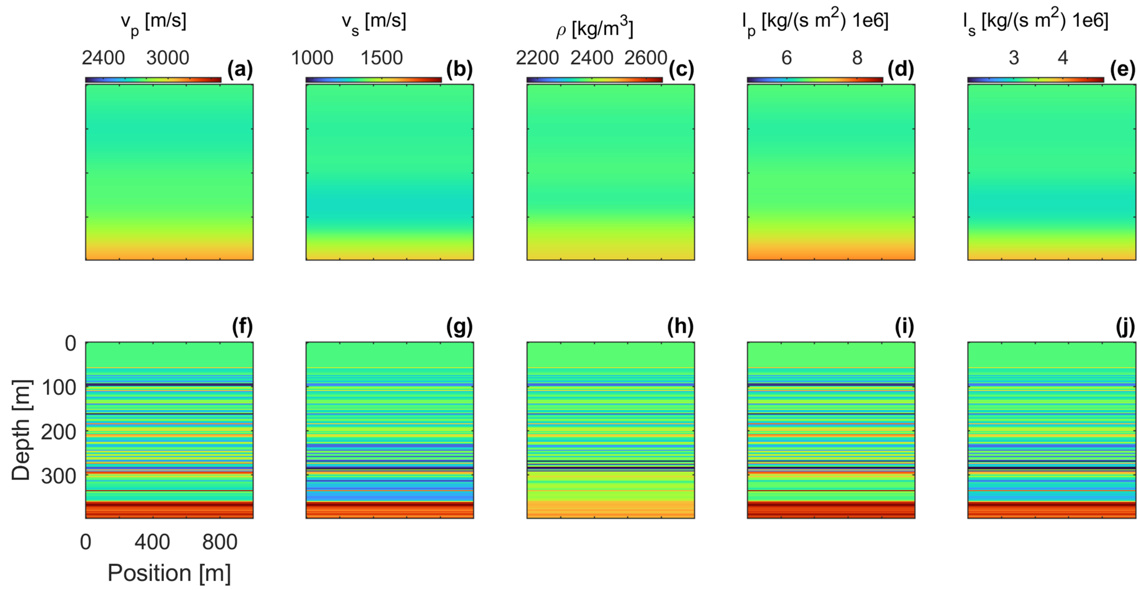

FIG. 8. Starting models for (a) V_p, (b) V_s, (c) ρ, (d) I_p, and (e) I_s. Baseline models pre-injection for (f) V_p, (g) V_s, (h) ρ, (i) I_p, and (j) I_s

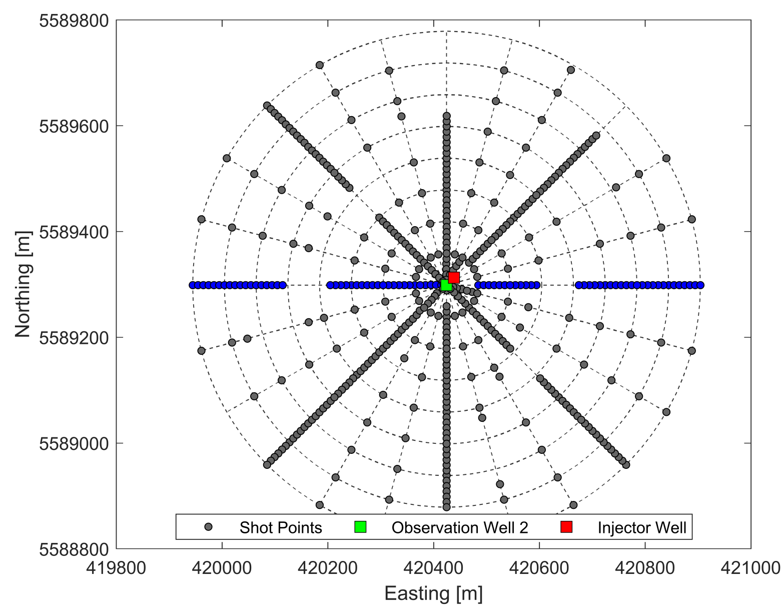

FIG. 9. Source geometry for the 2018 walkaway-walkaround VSP. Shot points are marked by the gray circles and are centered on observation well two marked by the green square. The injector well is marked by the red square. The line selected for synthetic testing is highlighted by the blue dots.

density at both reflection and transmission angles leading to a more stable inversion. This I_p-I_s-rho parameterization also provides the best correlation between the true and inverted models in the deeper sections of the model below the last receiver at 324 meters. These findings support the hypothesis proposed when examining the radiation patterns.

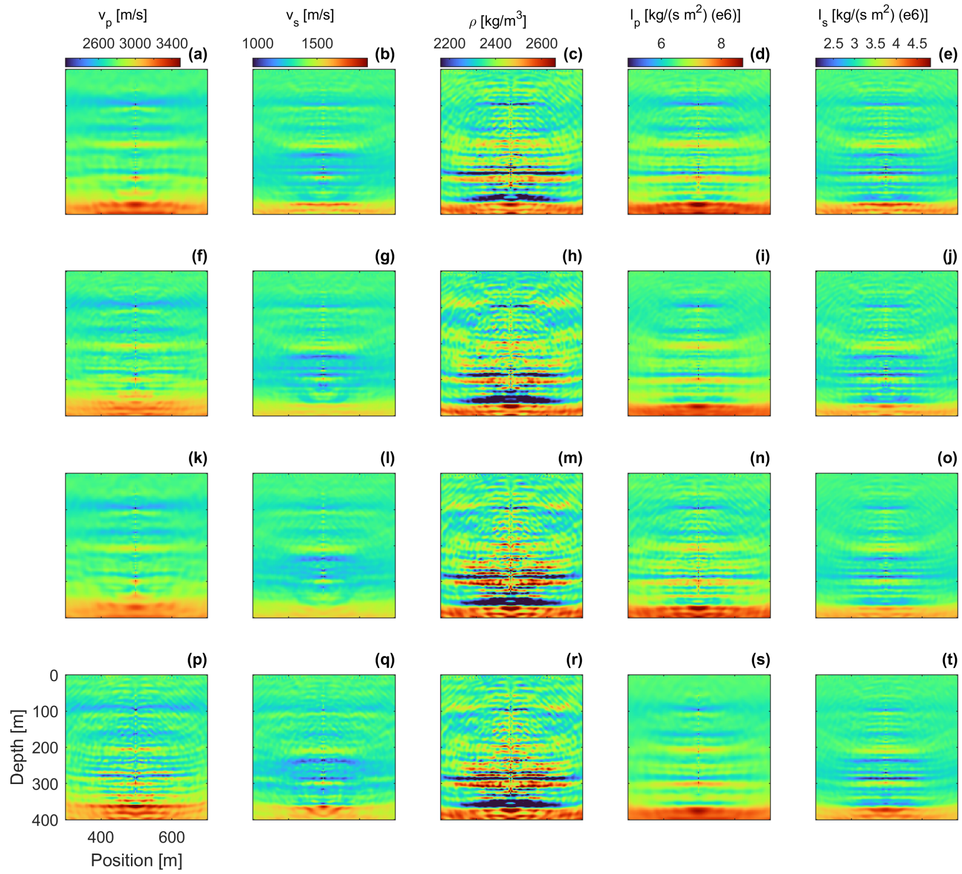

FIG. 10. Inversions from geophone data for V_p, V_s, ρ,I_p, and I_s for the V_p-V_s-ρ parameterization (a)-(e), V_p-V_s-I_p parameterization (f)-(j), V_p-V_s-I_s parameterization (k)-(o), and I_p-I_s-ρ parameterization (p)-(t).

Figures 12(a)-12(e) plot the inverted models for V_p, V_s, ρ, I_p, and I_s for data from the straight fiber for the $1/V_p^2$-$1/V_s^2$-ρ parameterization, Figures 12(f)-12(j) for the V_p-V_s-I_p parameterization, Figures 12(k)-12(o) for the V_p-V_s-I_s parameterization, and Figures 12(p)-12(t) for the I_p-I_s-ρ parameterization. Figure 13(a)-13(e) compares the inverted models for the $1/V_p^2$-$1/V_s^2$-ρ (green) and I_p-I_s-ρ (red) at the well location, and Figure 13(a)-13(e) compares the inverted models for the V_p-V_s-I_p (magenta) and V_p-V_s-I_s (blue). The lack of sensitivity to the ϵ_{xx} and ϵ_{xz} components of the strain field result in a marked degradation in the inversion results from the data supplied by straight fibers as compared to the inversion from the geophone data, and exposes the inversions to stronger cross-talk as evident in figure 13h. This is a result of the scattering patterns being more strongly correlated when we only have sensitvity to a portion of the scattered wavefield. Figures 3j, 3o, 3t, show that when only a portion of the scattered wavefield is sensed, the radiation patterns can be strongly correlated. However, when the sensitivity to the ϵ_{xx} component of strain is enhanced, through for example a helical wind, the increased sensitivity leads to a stronger decoupling of the radiation patterns.

Figures 14(a)-14(e) plot the inverted models for V_p, V_s, ρ, I_p, and I_s for data from the helical fiber for the $1/V_p^2$-$1/V_s^2$-ρ parameterization, Figures 14(f)-14(j) for the V_p-V_s-I_p

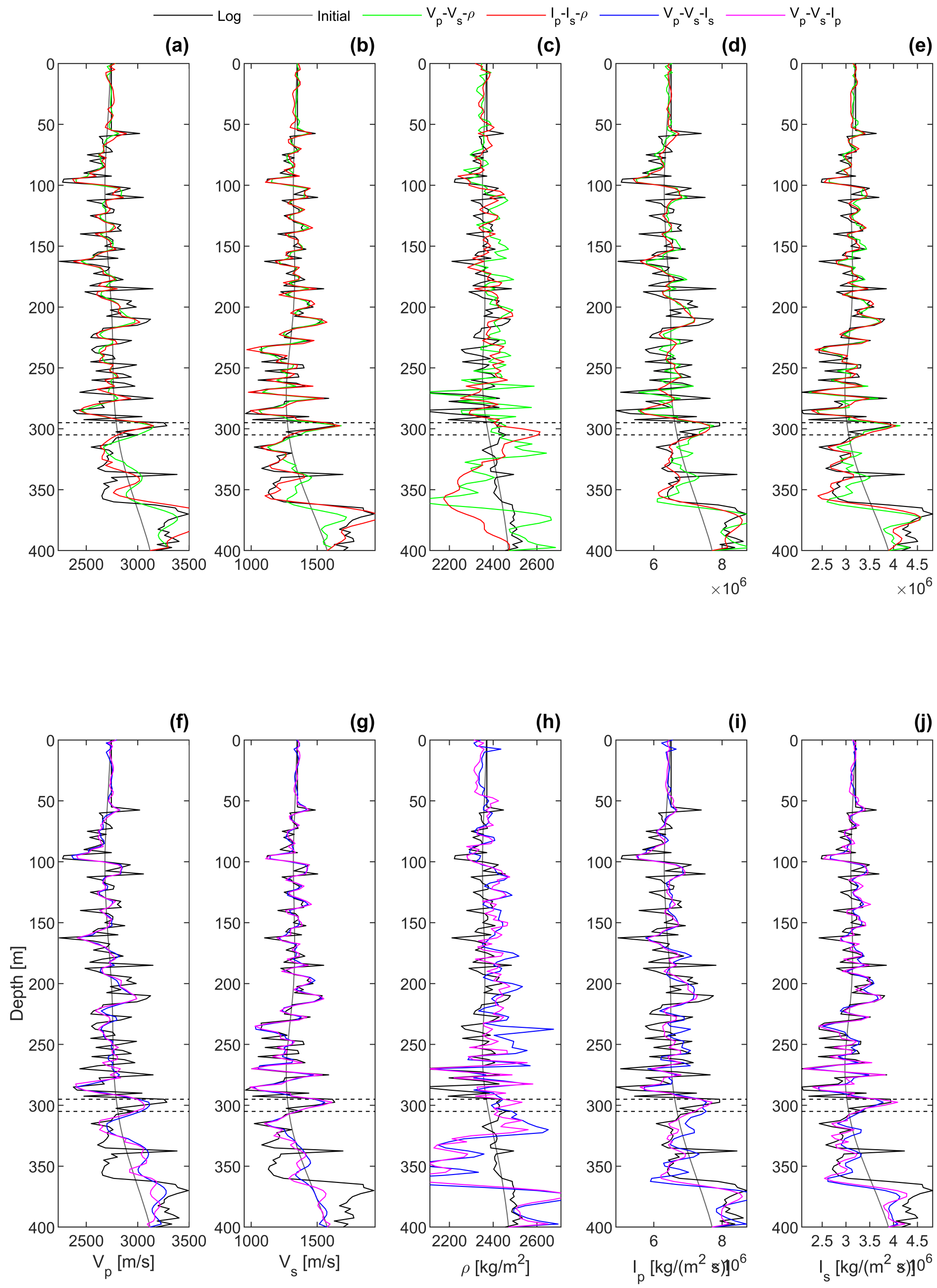

FIG. 11. (a)-(e) Comparison between V_p-V_s-ρ and I_p-I_s-ρ parameterizations for inversions from geophone data in V_p, V_s, ρ,I_p, and I_s. (f)-(j) Comparison between V_p-V_s-I_p and V_p-V_s-I_s parameterizations for inversions in V_p, V_s, ρ,I_p, and I_s.

parameterization, Figures 14(k)-14(o) for the V_p-V_s-I_s parameterization, and Figures 14(p)-14(t) for the I_p-I_s-ρ parameterization. Figure 15(a)-15(e) compares the inverted models for the $1/V_p^2$-$1/V_s^2$-ρ (green) and I_p-I_s-ρ (red) at the well location, and Figure 15(a)-15(e) compares the inverted models for the V_p-V_s-I_p (magenta) and V_p-V_s-I_s (blue). The enhanced

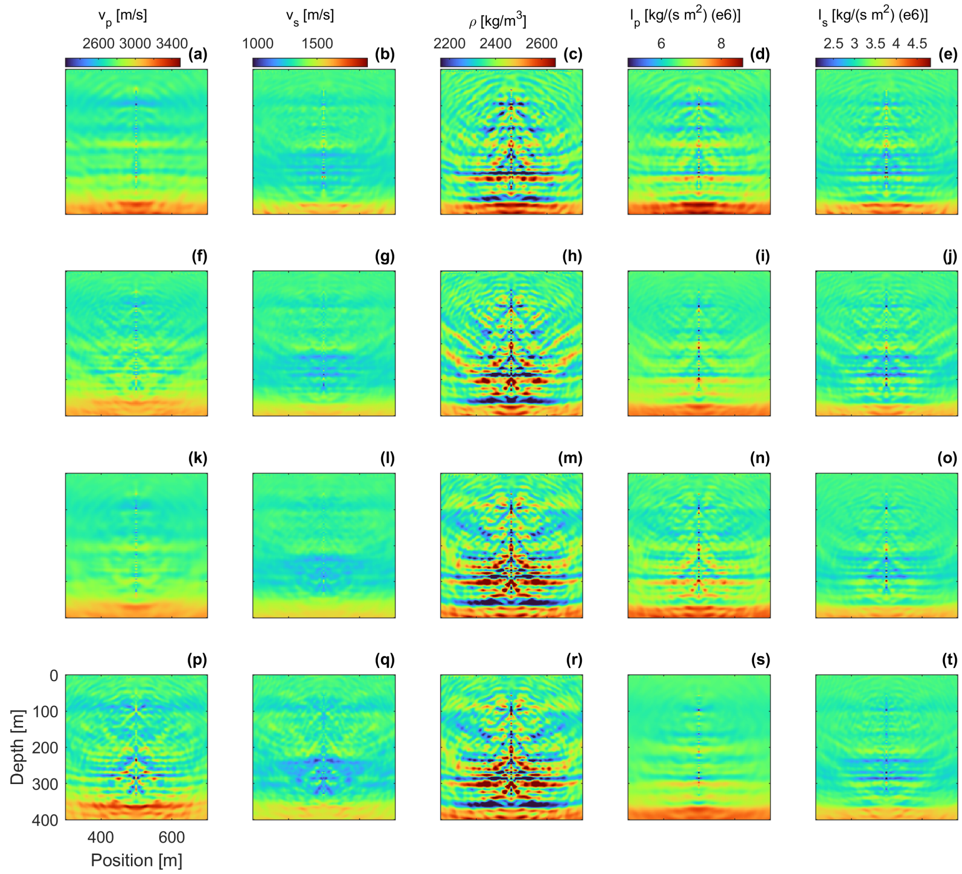

FIG. 12. Inversions from straight fiber data for V_p, V_s, ρ,I_p, and I_s for the V_p-V_s-ρ parameterization (a)-(e), V_p-V_s-I_p parameterization (f)-(j), V_p-V_s-I_s parameterization (k)-(o), and I_p-I_s-ρ parameterization (p)-(t).

sensitivity provided by the helical fiber reduces cross-talk and produces more robust inversions compared to the straight fiber. Overall, the inversion from the I_p-I_s-ρ parameterization also show the best cross-talk suppression and provide the strongest correlation between the true and inverted models at the well location for the straight and helical fibers.

Macquet et al. (2019) analyzed the effect injection of CO_2 had on the reservoir properties V_p, V_s and ρ for one year of injection and five years of injection for rate of one tonne per day of injection. Figure 16a-16e plot the change in V_p, V_s, ρ, I_p, and I_s models over five years of injection. Data were generated from the models computed after five years of injection using the same frequency and acquisition as the baseline models. Using the inverted models from the baseline datasets as the starting models, the datasets from the post injection models were inverted using the same inversion scheme. Figures 16f-16j plot the inverted change in V_p, V_s, ρ, I_p, and I_s for data acquired with geophones, where the change in each parameter was computed by subtracting the inverted models from the baseline data from the inverted models from the simulated dataset post injection. Figures 16k-16o and Figures 16p-16t plot the change in V_p, V_s, ρ, I_p, and I_s for straight and helical DAS fiber data respectively.

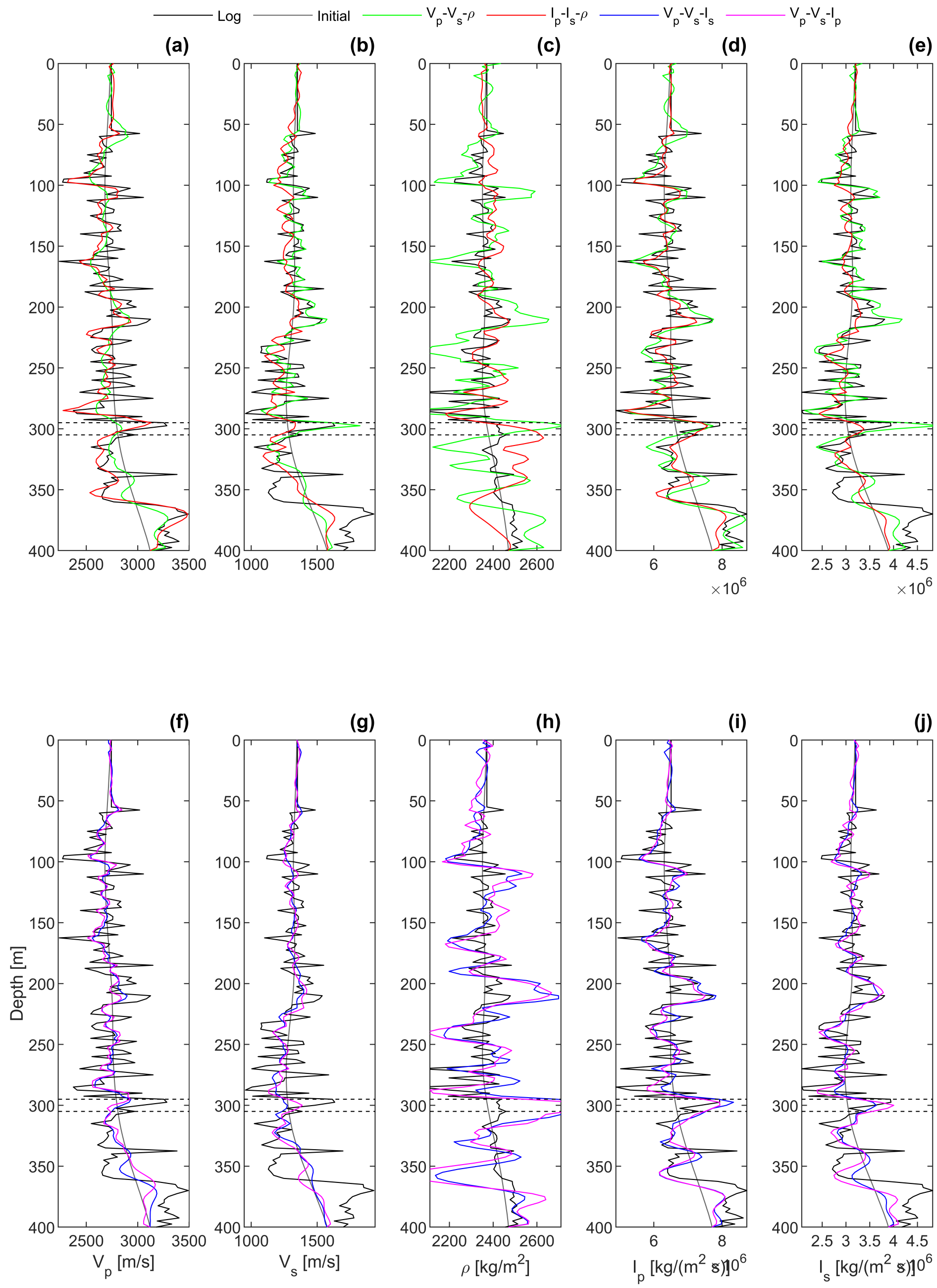

FIG. 13. (a)-(e) Comparison between V_p-V_s-ρ and I_p-I_s-ρ parameterizations for inversions from straight fiber data in V_p, V_s, ρ,I_p, and I_s. (f)-(j) Comparison between V_p-V_s-I_p and V_p-V_s-I_s parameterizations for inversions in V_p, V_s, ρ,I_p, and I_s.

The inversion results for the V_p and I_p anomalies are largely reasonable using data from all three acquisition technologies. The spatial extent and amplitude of the anomalies are well characterized by the inversion. The inversions for V_s and I_s do suggest an anomaly in the correct reservoir formation, but also suggest other spurious anomalies, especially in the

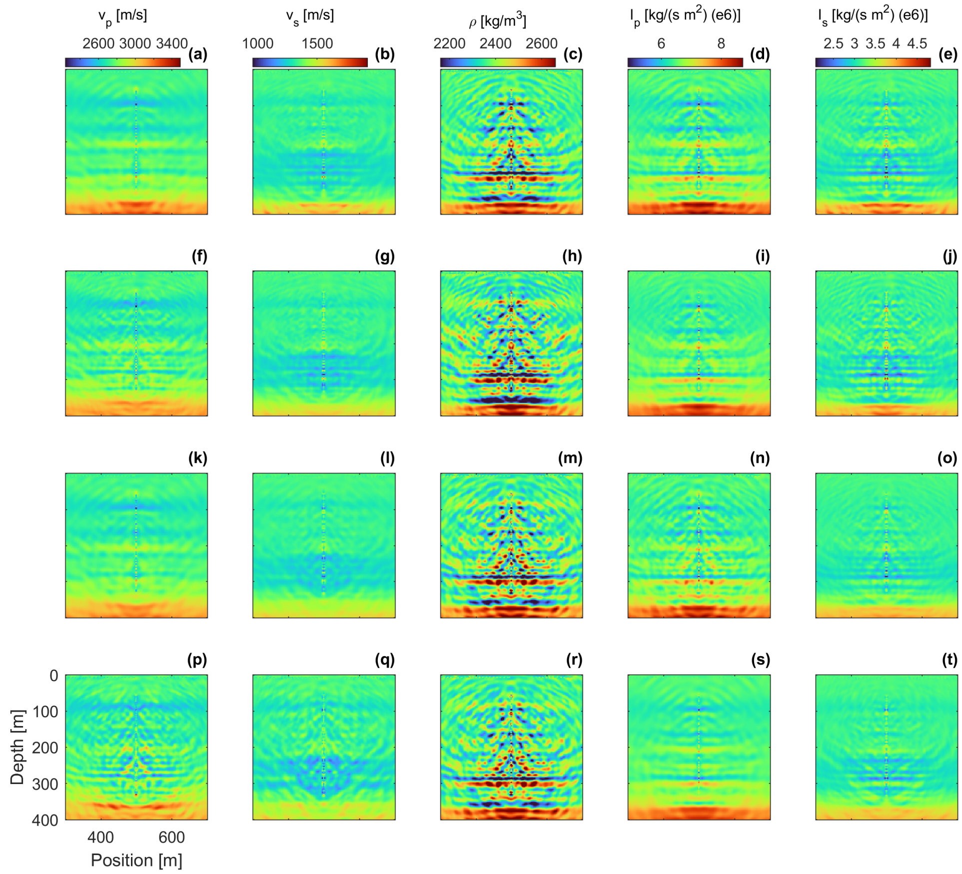

FIG. 14. Inversions from helical fiber data for V_p, V_s, ρ,I_p, and I_s for the V_p-V_s-ρ parameterization (a)-(e), V_p-V_s-I_p parameterization (f)-(j), V_p-V_s-I_s parameterization (k)-(o), and I_p-I_s-ρ parameterization (p)-(t).

deeper sections. We propose two possible reasons for this, (1) when inverting the baseline models the inversion should have been run for more iterations allowing for better characterization of the background medium, (2) the anomaly, being much smaller in amplitude than the V_p anomaly does not produce sufficient change in the data to be well characterized. The inversion for density is quite poor for all three acquisitions. While injection of CO_2 produces a large ($\approx$ -30%) change in V_p it induces a very small change ($\approx$ -0.8%) in density. This very small change in density is hard to invert for and becomes masked by larger updates if the baseline model is not a near perfect characterization of the background medium. Additionally, in field inversions it is expected that any change in acquisition, near surface conditions, or shot placement would make it challenging to invert for the relatively small density anomaly.

CONCLUSIONS

In this paper we set out to examine the expectation we may have for our results when inverting data from the 2018 walkaway-walkaround VSP dataset acquired at the CaMI field research station. Using well logs from the injector and geophysics observation well we constructed baseline models for V_p, V_s, and ρ. Simulated geophone, straight DAS fiber,

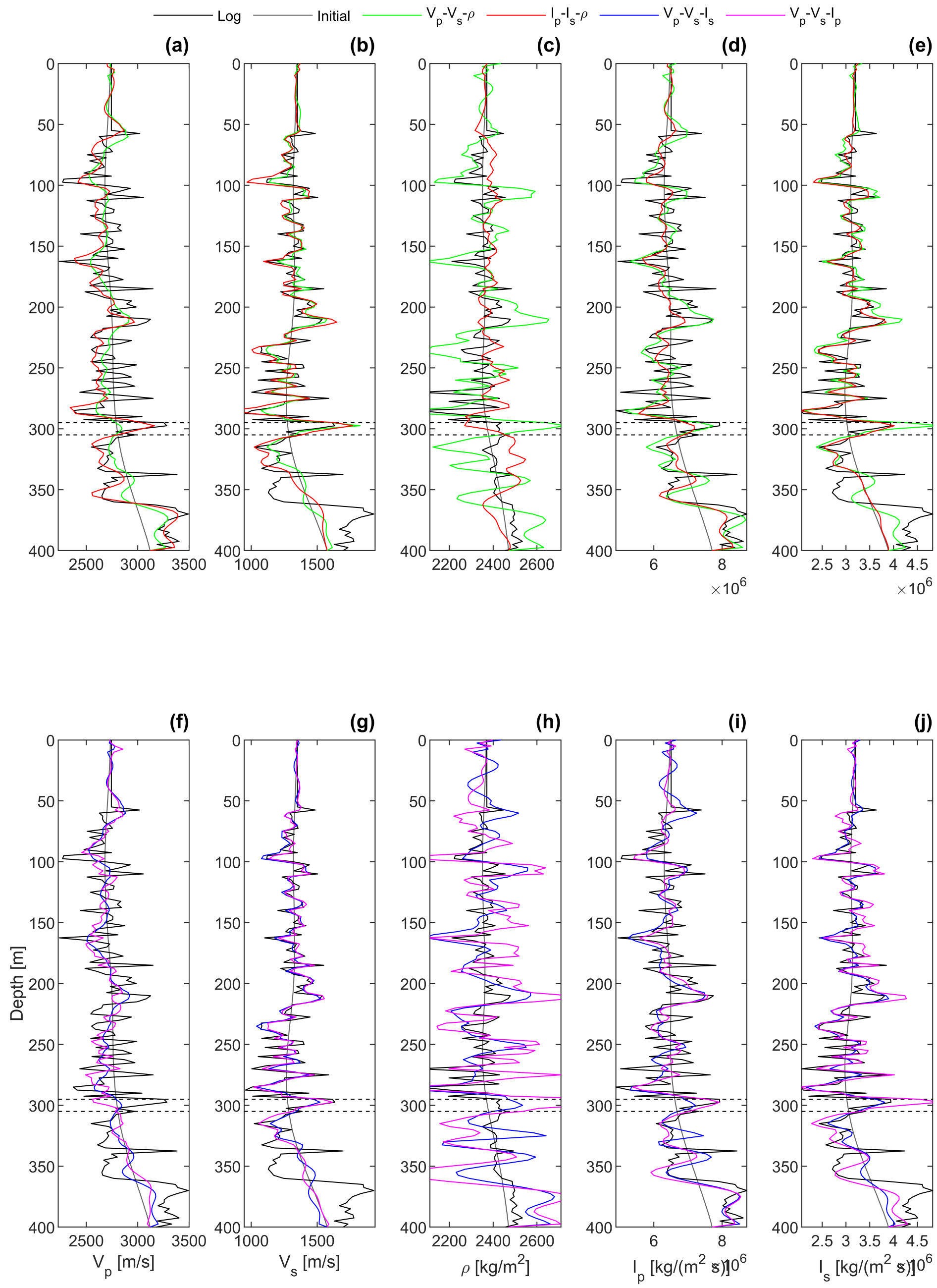

FIG. 15. (a)-(e) Comparison between V_p-V_s-ρ and I_p-I_s-ρ parameterizations for inversions from helical fiber data in V_p, V_s, ρ,I_p, and I_s. (f)-(j) Comparison between V_p-V_s-I_p and V_p-V_s-I_s parameterizations for inversions in V_p, V_s, ρ,I_p, and I_s.

and 30-degree helical DAS fiber data from these baseline models were then inverted using $V_p - V_s - \rho$, $V_p - V_s - I_p$, $V_p - V_s - I_s$, and $I_p - I_s - \rho$ parameterizations. Analysis of radiation patterns suggested that the $I_p - I_s - \rho$ parameterization would likely produce the most robust inversions, while mitigating cross-talk. Inversions confirmed this hypoth-

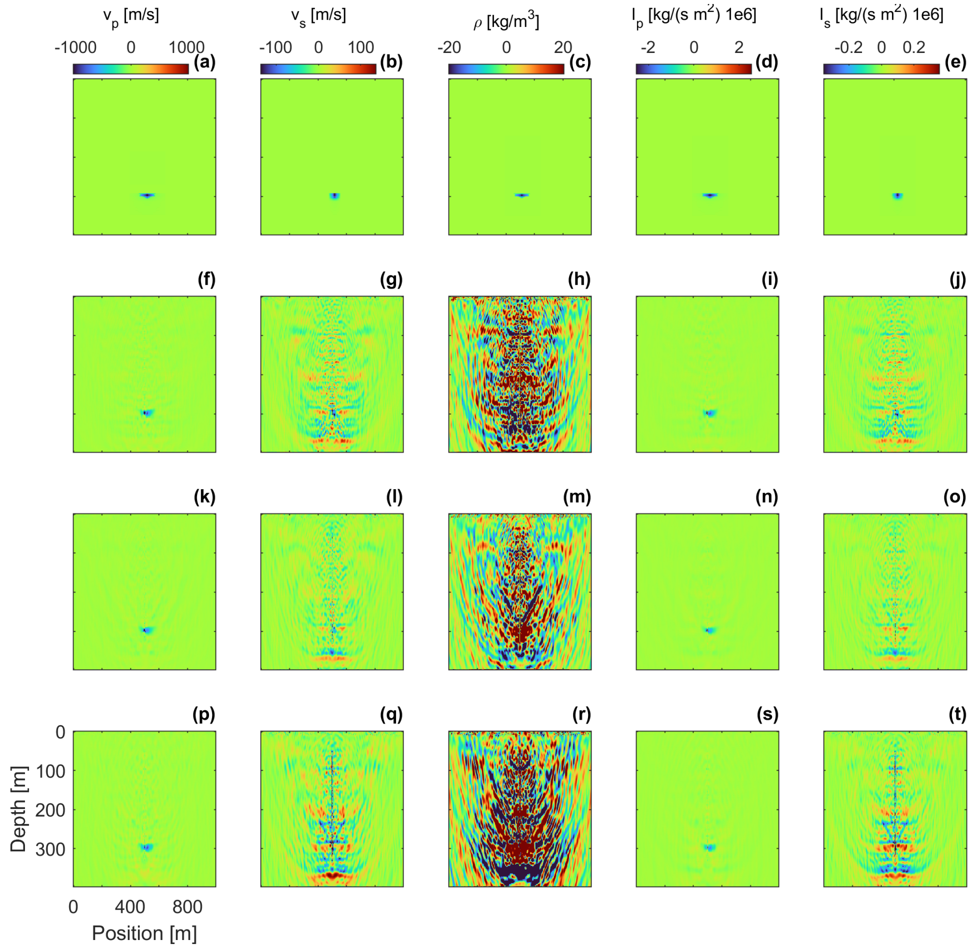

FIG. 16. (a)-(e) Difference between baseline models from Figures 8a-8e and the models computed by Macquet et al. (2019) after 5 years of injection for V_p, V_s, ρ, I_p, and I_s. Difference between inverted models using data from the true baseline models and data from the models after 5 years of injection using the $I_p - I_s - \rho$ parameterization for (f)-(j) geophones, (k)-(o) straight fiber, and (p)-(t) helical fiber. Column one plots the inverted models for V_p, column 2 for V_s, column 3 for ρ, column 4 for I_p, and column 5 for I_s

esis. Post-injection models were then used to generate post-injection datasets. Using the inverted baseline models as starting models, inversions were computed for data from the post-injection models. All three acquisitions were able to invert for the V_p/I_p anomalies but struggled to invert for V_s/I_s and ρ. The results derived here from synthetic tests provide insights into how to proceed with inverting the VSP field data.

ACKNOWLEDGMENTS

The authors would like to thank the sponsors of the CREWES project as well NSERC under the grants CRDPJ 461179-13 and CRDPJ 543578-19 for making this work possible through their financial support. Matt Eaid and Scott Keating were partially supported through scholarships from the SEG foundation.

REFERENCES

Bacci, V., OB́rien, S., Frank, J., and Anderson, M., 2017, Using a walk-away DAS time-lapse VSP for CO2 plume monitoring at the Quest CCS Project: CSEG Recorder, **42**, No. 3.

Eaid, M., Li, J., and Innanen, K., 2018, Modeling the response of shaped-DAS fibres to microseismic moment tensor sources: SEG Expanded Abstracts.

Eaid, M. V., Keating, S. D., and Innanen, K. A., 2020, Multi-parameter seismic elastic full waveform inversion with combined geophone and shaped fiberoptic cable data: GEOPHYSICS, **0**, No. 6, 1–66.

Gordon, A., and Lawton, D., 2018, Walk away VSP processing of DAS and geophone data at CaMI Field Research Station, Newell County, Alberta: CREWES Research Reports, **30**, No. 12, 1–22.

Innanen, K., and Eaid, M., 2017, Design of das fibres for elastic wave mode discrimination: CREWES Research Reports, **29**, No. 35.

Lawton, D., Osadetz, K., and Saeedfar, A., 2017, CCS monitoring technology innovation at the CaMI Field Research Station, Alberta, Canada: European Association of Geoscientists and Engineers Expanded Abstracts.

Macquet, M., Lawton, D. C., Saeedfar, A., and Osadetz, K. G., 2019, A feasibility study for detection thresholds of co2 at shallow depths at the cami field research station, newell county, alberta, canada: Petroleum Geoscience, **25**, No. 4, 509–518.

Marfurt, K. J., 1984, Accuracy of finite-difference and finite-element modeling of the scalar and elastic wave equations: Geophysics, **49**, 533–549.

Metivier, L., Brossier, R., Virieux, J., and Operto, S., 2013, Full waveform inversion and the truncated newton method: Siam J. Sci. Comput., **35**, B401–B437.

O'Brien, S., 2017, The Quest CCS Project - MMV Technology Deployment Through Two Years of Operation, *in* AGU Fall Meeting Abstracts, vol. 2017, S54A–01.

Pan, W., Innanen, K. A., Geng, Y., and Li, J., 2019, Interparameter trade-off quantification for isotropic-elastic full-waveform inversion with various model parameterizations: Geophysics, **84**, No. 2, R185–R206.

Pratt, R., 1990, Frequency-domain elastic wave modeling by finite differences: A tool for crosshole seismic imaging: Geophysics, **55**, No. 5, 514–639.